The $O(^1D)$ yield from O_2 photodissociation near H Lyman-α (121.6 nm)

J. Lacoursière, S. A. Meyer,[a] G. W. Faris, and T. G. Slanger
Molecular Physics Laboratory, SRI International, Menlo Park, California 94025

B. R. Lewis and S. T. Gibson
Research School of Physical Sciences and Engineering, The Australian National University, Canberra, ACT 0200, Australia

(Received 4 September 1998; accepted 20 October 1998)

The solar H Lyman-α line is, through O_2 photodissociation, an important source of $O(^1D)$ production throughout the mesosphere and lower thermosphere. To ascertain the energy balance in this altitude region, it is necessary to know the $O(^1D)$ yield across the solar H Lyman-α feature, since H Lyman-α absorption by O_2 at $\sim$80 km accounts for a substantial fraction of the solar radiation absorbed in the mesosphere. An earlier laboratory study had provided a value of 0.44 ± 0.05 for the $O(^1D)$ yield at the center of the solar H Lyman-α line, where the profile shows a minimum in intensity due to strong self-reversal of the line. Using tunable laser radiation, we have determined the $O(^1D)$ yield from O_2 photodissociation across the entire H Lyman-α profile from 121.2 to 121.9 nm, at a spectral resolution of 0.0015 nm (1 cm^{-1}). The results reveal a strongly wavelength-dependent window in the $O(^1D)$ yield, the origins of which are explained using calculations based on a coupled-channel Schrödinger-equations model of the O_2 photodissociation. The calculations, which show significant isotopic dependence near H Lyman-α, predict that the depth of the quantum-yield window will increase significantly as the temperature is lowered.
 [S0021-9606(99)00604-2]

I. INTRODUCTION

The coincidence in wavelength between the H Lyman-α line ($\lambda=121.6$ nm) and a deep window in the O_2 photoabsorption cross section has important consequences for the photochemistry of the terrestrial atmosphere. Atmospheric photodissociation of O_2 by solar Lyman-α radiation[1] contributes an important fraction of the total $O(^1D)$ production in the 75–82 km altitude region, with the remainder coming from O_3 photodissociation in the 200–300 nm Hartley band.[2] Schumann-Runge (SR) band absorption leads exclusively to $O(^3P)+O(^3P)$ products, whereas it has been known since the work of Lee *et al.*[3] that the quantum yield for $O(^1D)$ at Lyman-α is 0.44 ± 0.05.

Whether $O(^1D)$ or $O(^3P)$ is generated in a particular altitude region is an important question, as it affects both the chemistry and the energy balance in that region. The chemical reactivities of $O(^1D)$ and $O(^3P)$ are quite dissimilar, and the details of the processes by means of which the electronic energy of $O(^1D)$ and the translational energy of $O(^3P)$ are dissipated are also distinct. It is therefore essential to determine the yield of $O(^1D)$ at Lyman-α, and it is particularly important in an experimental determination to use radiation that has narrow-enough bandwidth to allow measurement of the wavelength dependence of the yield within the peculiar solar Lyman-α line shape.

Figure 1 shows the solar Lyman-α profile as parametrized by Chabrillat and Kockarts,[4] together with the O_2 absorption cross section at room temperature measured by Lewis *et al.*[5] The area of this Lyman-α profile is the usual value, $\Phi_\infty=3\times10^{11}$ photons $cm^{-2}\,s^{-1}$, which is representative of a quiet-Sun activity level.[6,7] The line has a minimum of intensity at line center due to absorption by geocoronal hydrogen.[8] The full width at half-maximum (FWHM) of the line is 0.08 nm (54 cm^{-1}) and the flux at its center is about one-quarter of its peak value. In the laboratory, a typical hydrogen-discharge lamp has an unreversed, or only slightly reversed, Lyman-α profile which is typically 0.0015 nm wide. To the extent that the $O(^1D)$ yield may vary across the 0.08 nm solar linewidth, conclusions about atmospheric $O(^1D)$ processes based on laboratory data obtained using such a source could be suspect. In the work of Lee *et al.*,[3] a value of 0.44 ± 0.05 was reported for the $O(^1D)$ yield at Lyman-α, obtained using a laboratory hydrogen-discharge lamp source. In the 120–130 nm spectral region, it was observed that the $O(^1D)$ yield showed sharp variations. However, it remains unclear whether the measured yield is relevant to O_2 photodissociation by actual solar Lyman-α, since the laboratory determination was made at exactly Lyman-α, i.e., in the core of the Lyman-α profile where the solar irradiance has a minimum. It was thus necessary to develop a light source with a tunability range of at least 0.1 nm, so that the entire width of the solar Lyman-α profile could be investigated. For that purpose, we used a tunable vacuum-ultraviolet (VUV) pulsed-laser light source with a bandwidth of ~1 cm^{-1} (0.0015 nm) FWHM and a tunability >10 nm. This source was designed by Meyer and Faris[9] and will be described briefly in Sec. II.

Selected potential-energy curves for O_2 are shown schematically in Fig. 2. When O_2 is excited from its ground state $X\,^3\Sigma_g^-$ into the so-called ''window region'' (110–130 nm,

[a]Present address: Tech Semiconductor, Woodlands, P.O. Box 0353, Singapore 917302.

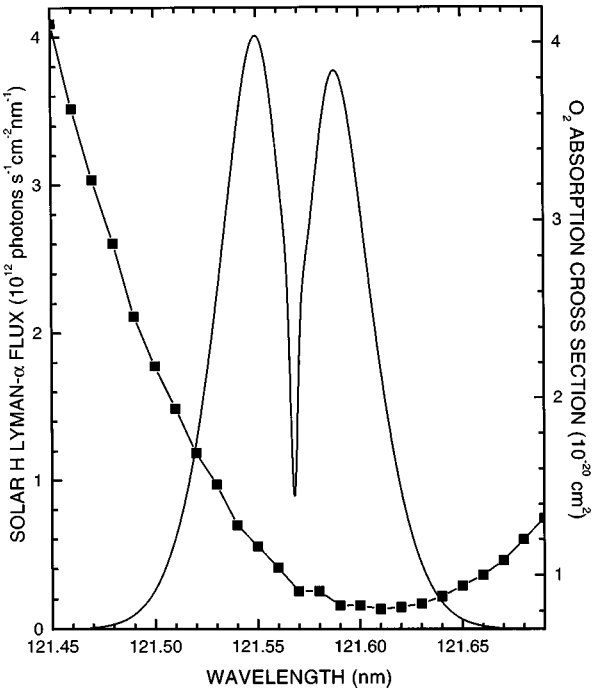

FIG. 1. Detailed view of the solar Lyman-α profile (the solid line, left axis), as parametrized by Chabrillat and Kockarts (Ref. 4) for a quiet-Sun activity level, showing its position near the minimum of the O_2 photoabsorption cross section (Ref. 5, connected squares, right axis).

9.6–11.4 eV),[10] an area of complex interactions between Rydberg and valence states, it is free to predissociate to a number of its lower dissociation limits. The energetically- and spin-allowed dissociation channels are

$$\begin{aligned} O_2(X\,^3\Sigma_g^-,\ v=0)+h\nu &\rightarrow O(^3P)+O(^3P)\\ &\rightarrow O(^3P)+O(^1D)\\ &\rightarrow O(^3P)+O(^1S), \end{aligned}$$

with dissociation thresholds of 242, 175, and 133 nm, respectively. In principle, fluorescence is also a possible relaxation mechanism, but Lee *et al.*[3] estimated from their experiment that the O_2 fluorescence yield after photoexcitation in this energy region was <0.001. Predissociation is therefore the dominant relaxation mechanism. Also, Ridley *et al.*[11] have determined experimentally an upper limit of 0.03 ± 0.01 for the $O(^3P)+O(^1S)$ dissociation yield at Lyman-α. Other works[12,13] have also reported a yield for this channel of <0.02, in general, between 116 and 125 nm. The channels $O(^3P)+O(^3P)$ and $O(^3P)+O(^1D)$ are, therefore, the only significant relaxation pathways available.[14]

The photoabsorption spectrum of O_2 in the window region is dominated by electric-dipole-allowed transitions from the $X\,^3\Sigma_g^-$ state into the strongly mixed Rydberg and valence states of $^3\Sigma_u^-$ and $^3\Pi_u$ symmetry. The $np\sigma_u\,^3\Pi_u$ states predissociate to the $O(^3P)+O(^3P)$ dissociation limit via the repulsive $\pi_g\,3\sigma_u\,^3\Pi_u$ valence state, and the $np\pi_u\,^3\Sigma_u^-$ states predissociate principally to the $O(^1D)+O(^3P)$ limit via the $\pi_u^3\pi_g^3\,B\,^3\Sigma_u^-$ valence state, the upper state of the SR transition. For comparison with the experimental results, we have also estimated theoretically the $O(^1D)+O(^3P)$ yield by performing a coupled-channel Schrödinger-equations

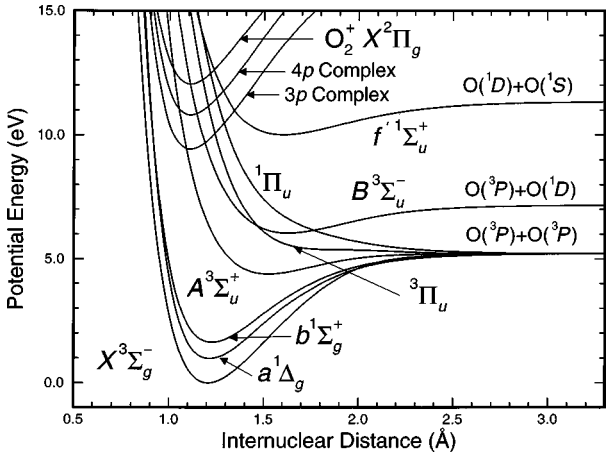

FIG. 2. Potential-energy curves of O_2, shown in a diabatic (crossing) representation. Energies are referred to the minimum in the ground-state $X\,^3\Sigma_g^-$ potential. The np Rydberg complexes, converging on the ionic ground state, contain $^{1,3}\Sigma_u^+$, $^{1,3}\Delta_u$, and $^{1,3}\Pi_u$ states.

(CSE) calculation of the partial $O_2\,^3\Sigma_u^- \leftarrow X\,^3\Sigma_g^-$ photodissociation cross section yielding $O(^1D)+O(^3P)$ and comparing it with the known experimental photoabsorption cross section.

This article is divided in two main sections: an experimental section (Sec. II), which includes a description of the data-analysis and presentation of the experimental results, and a theoretical section (Sec. III), where the $O(^1D)+O(^3P)$ quantum-yield calculation using the CSE method is described and compared with the experimental yield.

II. EXPERIMENT

A. $O(^1D)+O_2$ collisional energy transfer

We measured the relative $O(^1D)$ quantum yield from O_2 photodissociation between 121.2 and 121.9 nm at room temperature using O_2 of normal isotopic composition. The $O(^1D)$ population was monitored using the following energy-transfer reaction:

$$O(^1D)+O_2 \rightarrow O_2(b\,^1\Sigma_g^+,\ v=0,1)+O(^3P), \qquad (1)$$

where about 40% of the $O_2(b\,^1\Sigma_g^+)$ molecules are formed in the $v=1$ vibrational level and the remaining fraction in $v=0$.[15,16] There is strong evidence that the efficient removal of $O_2(b\,^1\Sigma_g^+,\ v=1)$ by O_2 ($k=1.5\times10^{-11}$ cm^3 s^{-1})[17] produces principally $O_2(b\,^1\Sigma_g^+,\ v=0)$,[17] which is deactivated very inefficiently by O_2 ($k=3.9\times10^{-17}$ cm^3 s^{-1}).[15] This enables one to use the fluorescence of the $b\,^1\Sigma_g^+ \rightarrow X\,^3\Sigma_g^-(0,0)$ transition at 762 nm as a measure of the $O(^1D)$ population. The radiative lifetime of the $b\,^1\Sigma_g^+(v=0)$ state is 11 s.[18] The reason for using reaction (1) for our measurement is that direct detection of $O(^1D)$ using the $O(^1D)\rightarrow O(^3P)$ emission at 630 nm is much more difficult since $O(^1D)$ has a radiative lifetime of 147 s (Ref. 18) and is deactivated very efficiently by O_2 ($k=4\times10^{-11}$ cm^3 s^{-1}).[15]

B. VUV generation

We photodissociated O_2 with tunable VUV laser light generated by a two-photon-resonant difference-frequency

(2PRDFM) mixing process using an ArF excimer laser and a Nd:YAG-pumped dye laser. Tuning of the VUV wavelength was provided by varying the dye-laser wavelength ($\nu_{VUV} = 2\nu_{ArF} - \nu_{dye}$). This VUV laser system has been described extensively in a recent article[9] and will be summarized here.

The ArF excimer-laser beam (10 Hz, ~20 mJ/pulse) and the Nd:YAG-pumped dye-laser beam (Coumarin 47, 10 Hz, ~9 mJ/pulse) were focused into a phase-matched gas mixture of H_2 and Kr (H_2:Kr=10:1) or Kr and Ar (Kr:Ar =1:4.1). The VUV generation efficiency was enhanced by tuning the ArF laser to a two-photon resonance of H_2 (103 487.08 cm^{-1}) when using the H_2:Kr mixture, or of Kr (103 363.43 cm^{-1}) when using the Kr:Ar mixture. For our measurements, the Kr:Ar mixture was necessary to generate VUV across the Lyman-α line because the use of H_2 produces H atoms which absorb VUV at that wavelength. The focal points of the two beams were spatially and temporally overlapped in the mixing cell whose exit window was a MgF_2 plano-convex lens ($R=20$ cm). The laser beams (VUV, ArF, and dye) struck the lens off-center and were thus dispersively separated (the lens also acted like a prism) in addition to being collimated over a distance of about 1.4 m *in vacuo*. At the end of this vacuum path, large (7 mm diam) and small (1.5 mm diam) apertures were used to select the VUV beam and suppress stray light from the ArF- and dye-laser beams. A red phosphor screen was used to locate the VUV beam and center it in the 1.5 mm aperture. The absolute intensity of the beam was eye-evaluated from the intensity of its spot on the phosphor screen. On the basis of a single measurement with a pyroelectric energy probe made immediately after the beam was observed on the phosphor screen, we estimated our VUV energy during this experiment to be <0.5 μJ/pulse. The relative VUV intensity was monitored between the 1.5 mm aperture and the O_2 flow cell by a solar-blind photomultiplier tube (PMT) (EMR model 542G-08-18) operated at 3.5 kV and mounted at right angles to the beam. This PMT has a CsI photocathode providing ~200× more sensitivity at Lyman-α than at the ArF wavelength (λ =193 nm). When the pulses from the dye and ArF lasers were not temporally overlapped, therefore preventing VUV production, the PMT did not generate any detectable signal. The output of the PMT was preamplified and fed to a boxcar averager, the dc output of which was voltage-to-frequency converted. In this form, the signal could be sent into the second channel of the photon counter used for the $O(^1D)$ yield measurement.

The VUV wavelength was tuned by varying the dye-laser wavelength manually via the position of its grating. We calibrated the VUV wavelength, and thus, indirectly, the dye-laser grating dial, using a VUV spectrometer and known VUV emission lines. We produced VUV emission lines around 120 nm by generating amplified spontaneous emission (ASE) in 50 Torr of H_2. When tuning the ArF laser to the $Q(1)$ line of the $E,F\,^1\Sigma_g^+ \leftarrow X\,^1\Sigma_g^+(6,0)$ two-photon transition of H_2, sufficient population was transferred from the ground state to produce ASE from the E,F state to the $B\,^1\Sigma_u^+$ state, and also subsequent ASE in the VUV from the B state to the ground state (the Lyman bands). First, we observed the $R(1)$ and $P(3)$ ASE lines of the $B\,^1\Sigma_u^+ \rightarrow X\,^1\Sigma_g^+(1,2)$ transition (83 438.44 and 82 909.46 cm^{-1}, respectively)[19] in order to calibrate the VUV spectrometer, and then VUV was produced using 2PRDFM. The VUV wavelength measured with the spectrometer defined the true dye-laser wavelength, since ν_{ArF} was tuned to a known two-photon resonance of H_2. This procedure yielded an accuracy of ± 0.01 nm (± 7 cm^{-1}) for VUV wavelengths near Lyman-α. The bandwidth of the VUV light is not known precisely, but is estimated to be on the order of 1 cm^{-1} (0.0015 nm) FWHM on the basis of a previous experiment using the same lasers and VUV generation scheme.[20]

C. O_2 flow cell

The VUV beam entered and exited the O_2 flow cell through MgF_2 windows situated 28 cm apart. Two pressure gauges (100 and 760 Torr ranges) measured the O_2 pressure in the cell. O_2 was flowed at 4.6 slpm (standard liters per minute) in order to prevent a build-up of O_3 concentration due to the production of O atoms from O_2 photodissociation. This is particularly important since the photodissociation of O_3 can lead to the production of $O(^1D)$ and $O_2(b\,^1\Sigma_g^+)$ via the spin-allowed dissociation channels $O(^1D)+O_2(a\,^1\Delta_g)$ and $O(^1D)+O_2(b\,^1\Sigma_g^+)$,[21] which have respective thresholds of 310.3 and 266.9 nm. Moreover, the O_3 to O_2 absorption cross-section ratio at Lyman-α is about 100. The use of a static cell is thus not acceptable for this experiment.

D. Fluorescence detection

Fluorescence at 762 nm from the $b\,^1\Sigma_g^+ \rightarrow X\,^3\Sigma_g^-(0,0)$ transition was detected in photon-counting mode by a cooled PMT (RCA C31034) operated at 1.9 kV and situated on the top face of the flow cell. From its point of emission in the center of the cell, the fluorescence passed successively through a fused-silica plano-convex lens ($f=5$ cm, 4 cm diam), a glass long-pass filter (Schott RG-715), and a Kodak Wratten 89-B filter. A spherical mirror ($R=3$ cm, 3.5 cm diam) was also placed at the bottom of the cell to enhance the fluorescence collection efficiency. The length of the VUV laser beam path seen by the PMT (the detection region) was 1.5 ± 0.5 cm. The distance between the beginning of this detection region and the entrance window of the flow cell was 8 ± 0.5 cm. The pulses from the PMT were preamplified 100× and sent to a dual-channel photon counter (Stanford SR400) whose second channel was used to measure the relative VUV intensity.

The $b\,^1\Sigma_g^+ \rightarrow X\,^3\Sigma_g^-(0,0)$ fluorescence counts were accumulated during a time gate open between 0.4 and 10.4 ms after the VUV laser pulse. The position and width of the time gate were determined by the lifetime of the $b\,^1\Sigma_g^+(v=0)$ state and the amount of stray light generated by the laser pulse. The fluorescence lifetime was measured in a simple preliminary laser-induced fluorescence (LIF) experiment. We excited the $b\,^1\Sigma_g^+ \leftarrow X\,^3\Sigma_g^-(1,0)$ transition of O_2 at 686.9 nm with a pulsed Nd:YAG-pumped dye laser and detected the $b\,^1\Sigma_g^+ \rightarrow X\,^3\Sigma_g^-(0,0)$ fluorescence at 762 nm. With 100 Torr of O_2 (99.995% purity) flowing in the cell, we observed a fluorescence lifetime of 2 ms, which is four times shorter than the value of 8 ms expected from the quenching of

$O_2(b\,^1\Sigma_g^+,\ v=0)$ by O_2.[15] We first thought that this shorter lifetime could be caused by water vapor or another contaminant coming from the O_2 cylinder. The rate constant for quenching of $O_2(b\,^1\Sigma_g^+,\ v=0)$ by H_2O is large enough ($k=5.4\times10^{-12}$ cm^3 s^{-1}) to cause this effect, at the specified impurity level for the O_2 cylinder. Since a longer fluorescence lifetime results in a better signal, we tried to condense the impurities by flowing O_2 through a bath of dry ice and isopropanol prior to its injection into the cell. Unfortunately, this lengthened the lifetime from 2 to only 2.2 ms. Interestingly, we also observed that the fluorescence lifetime depended on the flow cell used. The lifetime was 2 ms with the stainless-steel cell used for the experiment at Lyman-α, and only 0.83 ms with a black-anodized coated cell. It thus appears that most of the impurities shortening the fluorescence lifetime come from the cell walls, a black-anodized coating being a more efficient adsorber than stainless steel. As a precautionary measure during the experiment at Lyman-α, we installed a bath of dry ice and isopropanol between the mechanical pumping system and the output of the flow cell in order to trap pump-oil particles that might have been very efficient at quenching the $b\,^1\Sigma_g^+(v=0)$ state. We do not know, however, if this actually lengthened the fluorescence lifetime since the signal at Lyman-α was too low to permit an easy measurement.

In summary, with the setup described above, we detected an average of 13 O_2 $b\,^1\Sigma_g^+\rightarrow X\,^3\Sigma_g^-(0,0)$ fluorescence events per VUV laser shot, with an average signal-to-background ratio of 2.7. The background counts most probably originate from the typical reddish fluorescence produced when the VUV laser beam, and to a lesser extent the ArF stray light, traverse the MgF_2 windows of the cell.

E. Data acquisition

The intensity $S(\lambda)$ (counts per laser pulse) of the $b\,^1\Sigma_g^+\rightarrow X\,^3\Sigma_g^-(0,0)$ fluorescence signal at wavelength λ, which is proportional to the $O(^1D)$ quantum yield $\Phi_{^1D}(\lambda)$, is given by

$$S(\lambda)=\epsilon N_{\mathrm{abs}}(\lambda)\Phi_{^1D}(\lambda), \tag{2}$$

where ϵ is the $b\,^1\Sigma_g^+\rightarrow X\,^3\Sigma_g^-(0,0)$ fluorescence detection efficiency, and $N_{\mathrm{abs}}(\lambda)$ is the number of photons absorbed per laser pulse in the detection region. If the number of photons per laser pulse entering the cell at wavelength λ is $f(\lambda)$, $N_{\mathrm{abs}}(\lambda)$ will be given by

$$N_{\mathrm{abs}}(\lambda)=f(\lambda)\exp[-\sigma(\lambda)\rho l_0]\{1-\exp[-\sigma(\lambda)\rho l_1]\}, \tag{3}$$

where $l_0=8\pm0.5$ cm defines the preabsorption region, i.e., the length between the entrance of the cell and the beginning of the detection region, $l_1=1.5\pm0.5$ cm is the length of the detection region, $\sigma(\lambda)$ is the absorption cross section (cm^2 molecule^{-1}) of O_2 at wavelength λ, and ρ is the O_2 number density (molecules cm^{-3}).

One of the difficulties in measuring the $O(^1D)$ quantum yield in the Lyman-α region is the fact that the O_2 absorption cross section increases very steeply when moving away from its minimum value near 121.6 nm (Fig. 1). This fact has two consequences. First, the wavelength dependence of the O_2 $b\,^1\Sigma_g^+\rightarrow X\,^3\Sigma_g^-(0,0)$ fluorescence signal will depend not only on the wavelength dependence of the $O(^1D)$ yield, but also on the wavelength dependence of the O_2 absorption cross section, as shown by Eqs. (2) and (3). This dependence must be reflected in the data analysis. Second, it is clear that the pressure dependence of the signal intensity at a given wavelength will show a maximum. This is due to the tradeoff between having more absorbers in the detection region, and having more VUV power loss in the preabsorption region. As the VUV wavelength varies, the pressure giving the optimum signal will change due to the variation of the O_2 absorption cross section. Since our $b\,^1\Sigma_g^+\rightarrow X\,^3\Sigma_g^-(0,0)$ fluorescence signal was not very large, it was difficult to measure the $O(^1D)$ yield across and beyond the solar Lyman-α profile at constant O_2 pressure without losing the signal. We therefore measured the $O(^1D)$ yield over a given wavelength region, and then changed the pressure to measure the yield over another region.

TABLE I. Characteristics and experimental conditions for each wavelength region used in the $O(^1D)$ quantum-yield measurements.

Region	λ-range (nm)	$P(O_2)$ (Torr)	No. of points	Nonlin. medium	P(med.) (Torr)
1	121.48–121.64	144±6	9	Kr:Ar	100:410
2	121.45–121.67	144±6	9	Kr:Ar	100:410
3	121.65–121.91	87±1	14	H_2:Kr	200:20
4	121.79–121.86	87±1	6	H_2:Kr	200:20
5	121.24–121.54	29±1	12	H_2:Kr	100:10
6	121.42–121.50	87±1	3	H_2:Kr	100:10

The data were acquired in the following way. After having manually set the VUV wavelength to a given value, the fluorescence counts and the VUV level were accumulated simultaneously for 600 laser shots under each of the following conditions: (1) with O_2 flowing in the cell; (2) without O_2 in the cell; (3) without O_2 in the cell and with the ArF- and dye-laser pulses desynchronized, thus preventing VUV production; (4) with O_2 in the cell and the ArF- and dye-laser pulses desynchronized. Condition (1) measured the signal proportional to the $O(^1D)$ production, or "$O(^1D)$ signal." Condition (2) measured the fluorescence background, which varied linearly with the relative VUV intensity. Condition (3) allowed measurement of the background in the VUV channel. The comparison of the fluorescence counts in steps (3) and (4) was important because it confirmed that stray light from the ArF laser ($\lambda=193$ nm) was not intense enough to produce fluorescence from its absorption by O_2, or, potentially, O_3. The data were taken in segments of six overlapping wavelength regions. Table I lists for each wavelength region the O_2 pressure, the number of points, and the nonlinear medium used to generate the VUV light.

F. Data analysis

We measured the *relative* wavelength dependence of the $O(^1D)$ quantum yield, which is proportional to the absolute $O(^1D)$ yield, $\Phi_{^1D}(\lambda)$ of Eq. (2). In other words, we did not calibrate ϵ, the $b\,^1\Sigma_g^+\rightarrow X\,^3\Sigma_g^-(0,0)$ fluorescence detection efficiency. For each point of a given wavelength region, a

number directly proportional to $\Phi_{^1D}(\lambda)$ was extracted by normalizing the experimental signal $S(\lambda)$ using $N_{abs}(\lambda)$ [Eq. (3)]. In Eq. (3), the number $f(\lambda)$ of photons entering the cell per laser pulse was not measured, but was proportional to the measured relative VUV intensity I_{VUV}. From Eqs. (2) and (3), with $c(\lambda)=N_{abs}(\lambda)/f(\lambda)$ as the correction factor accounting for the variation of the absorption cross section of O_2, we obtain

$$\Phi_{^1D}(\lambda)\propto S(\lambda)/[c(\lambda)I_{VUV}]. \tag{4}$$

In the determination of $c(\lambda)$ we used the room-temperature O_2 absorption cross section of Lewis *et al.*,[5] corrected for pressure effects, for wavelength regions entirely contained between 121.4 and 121.9 nm (regions 1 and 2 in Table I), and the parametrized cross section of Dose *et al.*[22] for regions extending beyond this range (regions 3–6). The uncertainty of those cross sections is ~5%. With this correction procedure, the relative wavelength dependence of the $O(^1D)$ yield was determined within a single wavelength region. Since each of the six wavelength regions scanned partially overlapped the neighboring ones, the relative $O(^1D)$ yield across the entire wavelength range could be obtained by scaling the data so that they formed a single continuous curve.

On average, the uncertainty in the data points is ~8%, of which two-thirds arises from uncertainty in the correction factor $c(\lambda)$. An additional uncertainty of ~5% should be included to take into account the fact that the wavelength range of our experiment necessitated the use of experimental O_2 photoabsorption cross sections from two sources which differed slightly in their region of overlap.

G. Results and discussion

Our measured $O(^1D)$ quantum yields are shown in Fig. 3 and listed in Table II. The parametrized O_2 absorption cross section of Dose *et al.*[22] and the solar Lyman-α profile of Chabrillat and Kockarts[4] are reproduced in the bottom part of Fig. 3. The solid curve superimposed on the experimental data points is a Gaussian least-squares fit to equally weighted data points between 121.46 and 121.67 nm. It is important to recall that our yield measurements were not made absolutely. In the earlier study of Lee *et al.*,[3] it was possible to obtain a yield at Lyman-α relative to measurements in the Schumann–Runge continuum at 135–175 nm, where it is accepted that the $O(^1D)$ yield is unity. This was not possible in the present situation, with limited tunability of the laser system. We were therefore faced with two choices: either to use the earlier laboratory Lyman-α value, 0.44 ± 0.05, as a point of normalization, or to use the results of our calculations (Sec. III) which indicate that, as the photodissociation wavelength approaches the peak of the 120.6 nm ''second band'' of O_2, the yield should become unity. Fortunately, these two choices do not lead to very different final results. Because the short-wavelength yield appears to reach a limiting value at the same time as the absorption cross section is rapidly increasing toward the 120.6 nm peak, it seems reasonable to judge that this limiting value is, in fact, unity. By normalizing in this manner, the laboratory Lyman-α value, at 121.57 nm, is increased from 0.44 ± 0.05 to 0.53 ± 0.05, which we believe does not do injustice to the earlier work.

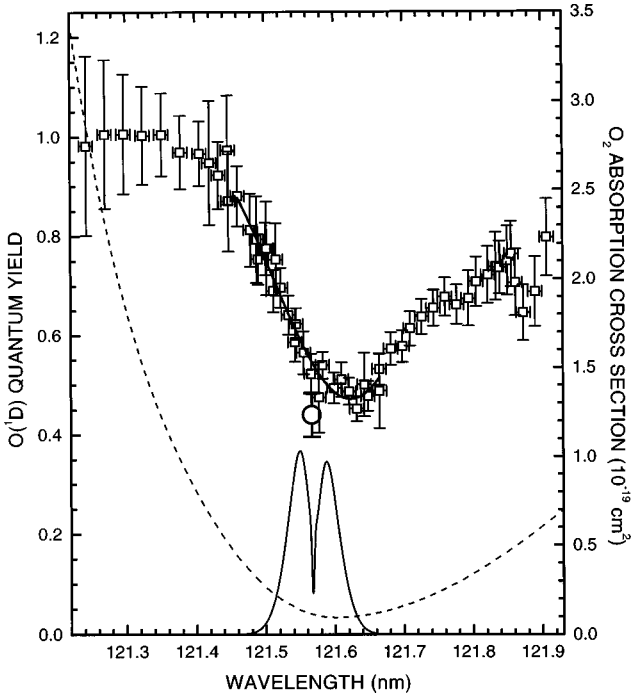

FIG. 3. Measured $O(^1D)$ quantum yield (squares, left axis). The parametrized O_2 absorption cross section of Dose *et al.* (Ref. 22, the dashed line, right axis) and the solar Lyman-α profile (Ref. 4) are reproduced in the bottom part of the figure. The solid line superimposed on the experimental data points is a Gaussian least-squares fit between 121.46 and 121.67 nm. The open circle is the previously measured value of 0.44 ± 0.05 for the $O(^1D)$ yield (Ref. 3).

The quantity of interest for modeling the $O(^1D)$ production rate by solar Lyman-α in the mesosphere and lower thermosphere (MLT) is the weighted-mean quantum yield $\langle\Phi_{^1D}\rangle$ given by

$$\langle\Phi_{^1D}\rangle=\frac{\int\Phi_{^1D}(\lambda)J(\lambda)d\lambda}{\int J(\lambda)d\lambda}=\frac{\int\Phi_{^1D}(\lambda)F(\lambda)\sigma(\lambda)d\lambda}{\int F(\lambda)\sigma(\lambda)d\lambda}, \tag{5}$$

where integration takes place over the solar Lyman-α profile. In Eq. (5), $J(\lambda)$ is the photolysis rate of O_2, given by the product $F(\lambda)\sigma(\lambda)$, where $F(\lambda)$ is the solar Lyman-α flux. It will be shown in Sec. III that the $O(^1D)$ quantum yield $\Phi_{^1D}(\lambda)$ is also a function of temperature, as is the O_2 absorption cross section $\sigma(\lambda)$.[5] In the MLT, the weighted-mean $O(^1D)$ yield will therefore depend on altitude via the temperature dependence of $\sigma(\lambda)$ and $\Phi_{^1D}(\lambda)$. Interestingly, the wavelength distribution of the solar Lyman-α flux $F(\lambda)$ is also a function of altitude. As pointed out by Nicolet,[23] the shape of the O_2 absorption cross section within the solar Lyman-α profile (Fig. 1) will generate stronger absorption of the low-wavelength half of the profile than of the high-wavelength half, thus deforming the profile as the light penetrates the atmosphere. This deformation will cause the weighted-mean $O(^1D)$ yield to decrease with decreasing altitude.

Given the purpose of this work, here we will limit ourselves to calculating the weighted-mean $O(^1D)$ quantum yield at room temperature using the O_2 absorption cross section of Lewis *et al.*,[5] the parametrized profile of Chabrillat

TABLE II. Experimental O(^1D) yield as a function of wavelength.

λ (nm)[a]	Region[b]	O(^1D) yield[c]	λ (nm)[a]	Region[b]	O(^1D) yield[c]
121.243	5	0.98±0.18	121.599	1	0.49±0.03
121.270	5	1.01±0.15	121.610	2	0.51±0.03
121.297	5	1.01±0.12	121.621	1	0.49±0.03
121.324	5	1.00±0.10	121.632	2	0.45±0.02
121.351	5	1.00±0.08	121.643	1	0.50±0.06
121.378	5	0.97±0.07	121.648	3	0.48±0.03
121.406	5	0.97±0.07	121.665	3	0.53±0.03
121.420	6	0.95±0.12	121.665	2	0.49±0.07
121.433	5	0.92±0.07	121.682	3	0.57±0.03
121.447	2	0.97±0.11	121.698	3	0.58±0.03
121.447	6	0.87±0.10	121.710	3	0.61±0.03
121.460	5	0.88±0.06	121.726	3	0.64±0.04
121.479	1	0.81±0.07	121.743	3	0.66±0.04
121.488	5	0.79±0.09	121.760	3	0.68±0.04
121.490	2	0.75±0.05	121.777	3	0.66±0.04
121.501	1	0.77±0.05	121.794	4	0.67±0.06
121.502	6	0.78±0.09	121.805	3	0.71±0.05
121.512	2	0.69±0.04	121.822	4	0.72±0.06
121.515	5	0.75±0.07	121.833	4	0.74±0.07
121.523	1	0.70±0.04	121.839	3	0.74±0.05
121.534	2	0.64±0.04	121.850	4	0.75±0.07
121.543	5	0.59±0.04	121.856	4	0.76±0.07
121.544	1	0.62±0.03	121.862	4	0.71±0.07
121.555	2	0.57±0.04	121.873	3	0.65±0.06
121.566	1	0.52±0.04	121.890	3	0.69±0.07
121.577	2	0.48±0.07	121.907	3	0.80±0.08
121.583	1	0.54±0.03			

[a]Wavelength calibration uncertainty ±0.01 nm (see the text).
[b]Scan region containing tabulated datum point (see Table I).
[c]Tabulated uncertainties are statistical, representing one standard deviation. An additional uncertainty of ~5% should be included to account for the use of two experimental O_2 photoabsorption cross sections which differ slightly in their range of overlap (see the text).

and Kockarts[4] representing the solar Lyman-α line shape at the top of the atmosphere, and our measured O(^1D) yield. The weighted-mean O(^1D) yield is calculated using Eq. (5), where the integration is performed on a grid defined by the experimental data points using the trapezoidal method. This calculation yields the result $\langle \Phi_{1D} \rangle = 0.58 \pm 0.06$. It is verified easily that the same value is obtained when using the fitted Gaussian O(^1D) yield shown in Fig. 3. This functional form of the yield, which may prove useful in atmospheric modeling, is given by

$$\Phi(\lambda) = 1.08 - \{0.168/[0.11(2\pi)^{1/2}]\} \times \exp\{-0.5[(\lambda - 121.623)/0.11]^2\}, \quad (6)$$

where λ is in the range 121.46–121.67 nm. It is also interesting to note that, when using only the numerator of Eq. (5), one finds that the low-wavelength half (λ<121.57 nm) of the solar Lyman-α profile at the top of the atmosphere (Fig. 1) produces two-thirds of the O(^1D) generated by the full solar Lyman-α line.

In addition to being consistent with the previous value of the yield at exactly Lyman-α, our experimental wavelength-dependent O(^1D) yield agrees well with the results of a semi-empirical CSE calculation. Section III explains how the calculations were performed and compares them with the experimental results.

III. THEORY

As implied in Sec. I, the total O_2 photodissociation cross section in the window region may be thought of as the sum of cross sections for the allowed transitions into the Rydberg-valence coupled $^3\Sigma_u^-$ and $^3\Pi_u$ states, the O(^1D) + O(^3P) photofragments arising entirely from $^3\Sigma_u^-$ dissociations. In Sec. III A, we model the O(^1D) + O(^3P) quantum yield in the window region near Lyman-α using the CSE method, and in Sec. III B the results are compared with our measured quantum yield.

A. Method of calculation

1. The CSE method

In the case of Rydberg and valence states of the same symmetry with molecular-orbital configurations differing in one or two of the occupied orbitals, such as the $^3\Pi_u$ and $^3\Sigma_u^-$ states of O_2, respectively, there may be strong interactions which invalidate the Born–Oppenheimer (BO) approximation.[24] This breakdown of the BO approximation may be addressed by using a CSE model in which the interactions between the BO basis states are included explicitly. In the adiabatic basis, the adiabatic potential-energy curves for the BO basis states exhibit an avoided crossing and these states interact nonadiabatically through an off-diagonal element of the nuclear kinetic-energy operator. In the diabatic basis, the diabatic BO basis-state potential-energy curves cross and interact through an off-diagonal element of the electrostatic Hamiltonian. Provided that a complete electronic-state basis is employed, then the results of CSE calculations are insensitive to the choice of an adiabatic or diabatic basis set. In practice, it is sufficient to include only enough interacting electronic states to accurately describe spectra in the energy region of interest. In this work, we choose the diabatic BO basis, as this has the attractive property that the wave functions, potential-energy curves, and coupling matrix elements can be expected to change smoothly with internuclear separation R.

The techniques of scattering theory[25] have been adapted to the calculation of molecular photodissociation cross sections. The CSE formalism, detailed by van Dishoeck *et al.*[26] and Torop *et al.*,[27] is particularly suitable for treatment of the strong Rydberg-valence interactions in O_2 and has been applied previously to explain unusual features in the spectrum of O_2.[28–31] Details of a CSE formulation suitable for the description of rovibronic photodissociation of O_2 have been given by Lewis *et al.*[29] Briefly, for a transition from a given rovibrational level of an initial uncoupled electronic state i into the n coupled states k, which include n_o open channels, the partial photodissociation cross section, in cm^2, to the open channel γ is given by

$$\sigma_{\gamma EJ \leftarrow iv''J''\Omega''} = 1.225 \times 10^{-23} g \nu \times |\langle \chi_{\gamma EJ}(R) | \mathbf{M} | \chi_{iv''J''\Omega''}(R) \rangle|^2, \quad (7)$$

and the total cross section by

$$\sigma_{EJ \leftarrow iv''J''\Omega''} = \sum_{\gamma=1}^{n_o} \sigma_{\gamma EJ \leftarrow iv''J''\Omega''}, \quad (8)$$

where E is the coupled-state energy, J is the rotational quantum number, ν is the transition energy in cm^{-1}, the degeneracy factor $g=(2-\delta_{0,\Lambda+\Lambda''})/(2-\delta_{0,\Lambda''})$, and the transition matrix elements are in atomic units. In Eq. (7), $\boldsymbol{\chi}_{\gamma EJ}(R)$ is the $n\times 1$ vector of coupled-channel radial wave functions with outgoing flux into channel γ, $\chi_{iv''J''\Omega''}(R)$ is the vibrational wave function of the initial state, and the elements of the $n\times 1$ rotronic transition-moment vector $\mathbf{M}$ are the products of appropriately normalized electronic transition moments $\mathcal{M}_k(R)$ and rotational matrix elements of the direction-cosine operator. The coupled-channel radial wavefunction vector $\boldsymbol{\chi}_{\gamma EJ}(R)$ is the solution of the diabatic-basis coupled Schrödinger equations, expressed in matrix form,

$$\left\{\mathbf{I}\frac{d^2}{dR^2}+\frac{2\mu}{\hbar^2}[E\mathbf{I}-\mathbf{V}(R)-\mathbf{V}^{\mathrm{rot}}(R)]\right\}\boldsymbol{\chi}_{\gamma EJ}(R)=0, \quad (9)$$

where μ is the molecular reduced mass, $\mathbf{I}$ is the identity matrix, $\mathbf{V}(R)$, of dimension $n\times n$, is the symmetric diabatic potential matrix, the diagonal elements of which are the diabatic electronic potential-energy curves $V_k(R)$, and $\mathbf{V}^{\mathrm{rot}}(R)$ is a diagonal matrix with elements given by matrix elements of the rotational part of the molecular Hamiltonian. The couplings between the interacting electronic states are given by the off-diagonal elements of $\mathbf{V}(R)$, containing the effects of electrostatic, rotational and spin-orbit interactions.

If the electronic wave functions are expressed in the Hund's case (a) e/f parity basis,[24] then the only nonzero elements $\mathcal{M}_k(R)$ arise from dipole-allowed parallel and perpendicular transitions between case (a) basis states and forbidden transitions borrow strength via the explicitly calculated upper-state mixing processes. For a finite temperature, the effective partial (or total) photodissociation cross sections can be expressed as the sums of cross sections into the upper-state e and f levels, each of which is calculated separately as a Boltzmann average of Eq. (7) [or Eq. (8)] over the initial distribution of v'',J'', and, in the case of a multiplet, Ω'' or F_i''.

2. The model implementation

In principle, the photodissociation of O_2 near Lyman-α at ~121.6 nm can be modeled by performing separate CSE calculations of the Rydberg-valence $^3\Pi_u \leftarrow X\,^3\Sigma_g^-$ and $^3\Sigma_u^- \leftarrow X\,^3\Sigma_g^-$ total photodissociation cross sections, which we denote as the ''Π'' and ''Σ'' cross sections, respectively. Since the Π_u dissociations yield only $O(^3P)+O(^3P)$ products, the total $O(^1D)+O(^3P)$ quantum yield would then be given by

$$\Phi_{^1D}(\lambda)=\sigma_{\Sigma_{^1D}}(\lambda)/[\sigma_\Sigma(\lambda)+\sigma_\Pi(\lambda)], \quad (10)$$

where $\sigma_{\Sigma_{^1D}}(\lambda)$ is the partial Σ cross section yielding $O(^1D)+O(^3P)$, denoted as ''$\Sigma_{^1D}$.'' However, significant uncertainties result in the Π cross section and the quantum yield determined in this way. The nearest identifiable $^3\Pi_u \leftarrow X\,^3\Sigma_g^-$ features in the O_2 spectrum occur at ~135.5 and ~116.2 nm, associated, respectively, with the lower and upper adiabatic states formed due to the strong $^3\Pi_u$ Rydberg-valence interaction.[28] In the extensive energy region between these states, which includes Lyman-α, the calculated CSE Π cross section becomes weak and oscillatory, and, in the absence of experimental information enabling refinement of the $^3\Pi_u$ model parameters pertinent to this region, cannot be regarded as reliable. On the other hand, the strong Σ cross section which dominates this region of the spectrum can be characterized well by a CSE treatment. Lyman-α lies between the longest and second bands of O_2,[32] at ~124.4 and ~120.6 nm, respectively, very strong predissociating resonances associated with the $v=0$ and $v=1$ levels of the $E\,^3\Sigma_u^-$ state, the upper adiabatic state resulting from the $^3\Sigma_u^-$ Rydberg-valence interaction. Therefore, in this work we calculate only the partial and total Σ cross sections, estimating the total $O(^1D)+O(^3P)$ quantum yield in the Lyman-α region using the expression

$$\Phi_{^1D}(\lambda)=\sigma_{\Sigma_{^1D}}(\lambda)/\sigma(\lambda), \quad (11)$$

where, as in Sec. II, $\sigma(\lambda)$ is the O_2 photoabsorption cross section. It is important to note that it is assumed implicitly in Eq. (11) that the cross sections $\sigma_{\Sigma_{^1D}}(\lambda)$ and $\sigma(\lambda)$ refer to the same isotopic variant or mixture of O_2. For most wavelengths, cross sections for O_2 of normal isotopic composition are indistinguishable from those for $^{16}O_2$. However, as will be seen in Sec. III B, this does not apply to the cross-section minimum near Lyman-α where it is essential to use a $\Sigma_{^1D}$ cross section properly corrected for isotopic effects before estimating $O(^1D)$ quantum yields using Eq. (11).

Our CSE model, optimized using experimental information over the 110.0–140.0 nm range, provides an accurate description of a large number of Σ_u features in the window region of the O_2 spectrum. A detailed description of the optimization of the model parameters is given elsewhere.[33] Briefly, the model includes the $n=3$ and $n=4$ Rydberg states and the lowest valence states of $^3\Sigma_u^-$, $^3\Sigma_u^+$ and $^1\Sigma_u^+$ symmetry, and takes into account Rydberg-valence couplings for each symmetry, $^3\Sigma_{u1}^- - {}^3\Sigma_{u1}^+$ and $^3\Sigma_{u0}^- - {}^1\Sigma_{u0}^+$ Rydberg–Rydberg spin-orbit couplings ($\sim 100\ cm^{-1}$), and **S**-uncoupling in the triplet states ($2B_\Sigma\sqrt{J(J+1)}$). The $^3\Sigma_u^+$ and $^1\Sigma_u^+$ states have been included to allow a description of the forbidden band systems, $3p\pi_u\, f\,^1\Sigma_u^+ \leftarrow X\,^3\Sigma_g^-$ and $3p\pi_u\, D\,^3\Sigma_u^+ \leftarrow X\,^3\Sigma_g^-$, which are visible in the window region. Within the framework of the CSE model, these forbidden systems occur by borrowing strength from the allowed $^3\Sigma_u^- \leftarrow X\,^3\Sigma_g^-$ transition through spin-orbit interactions between components of the $3p$ Rydberg complex. As will be seen in Sec. III B, the inclusion of the $^3\Sigma_u^+$ states is particularly important for an accurate estimation of the $O(^1D)$ quantum yield near Lyman-α, since the $np\pi_u\,^3\Sigma_u^+$ Rydberg states, which are spin-orbit-coupled to the isoconfigurational $^3\Sigma_u^-$ states, are predissociated by the $\pi_u^3\pi_g^3 A\,^3\Sigma_u^+$ state, the upper state of the Herzberg I system, which correlates with the $O(^3P)+O(^3P)$ limit. Thus, in certain narrow spectral regions the $O(^1D)$ quantum yield pertaining to the Σ spectrum will fall below the value of unity expected for pure $^3\Sigma_u^-$ predissociation. Our calculated cross sections were obtained, formally, by summing separate upper-state e-level and f-level calculations. The e-level block included the twelve diabatic states of $^3\Sigma_{u0}^-$, $^3\Sigma_{u1}^-$, $^3\Sigma_{u1}^+$, and $^1\Sigma_{u0}^+$ symmetry,

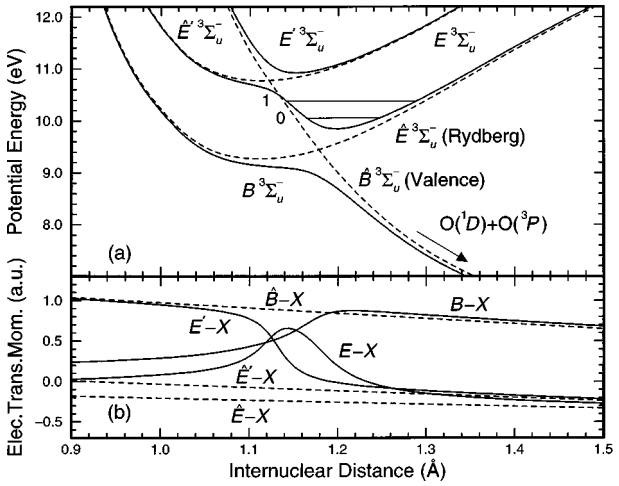

FIG. 4. (a) Diabatic CSE-model potential-energy curves $V_k(R)$ for the $^3\Sigma_u^-$ states of O_2 (dashed lines). The energy scale is defined relative to the minimum in the ground-state $X\,^3\Sigma_g^-$ potential-energy curve and the electronic-state nomenclature is discussed in Ref. 34. Strong Rydberg-valence coupling results in the corresponding adiabatic potential-energy curves (solid lines) exhibiting avoided crossings. The upper-state levels for the longest and second bands are indicated in relation to the adiabatic *E*-state potential, formed by the interaction of the pure valence and $n=3$ and $n=4$ Rydberg states. The Lyman-α region lies between these two levels. Predissociation of the *E* state occurs via the *B* state which correlates with the $O(^1D)+O(^3P)$ dissociation limit. (b) Diabatic CSE-model electronic transition moments $\mathcal{M}_k(R)$ for the $^3\Sigma_u^-\leftarrow X\,^3\Sigma_g^-$ transitions (dashed lines), together with the corresponding adiabatic moments (solid lines).

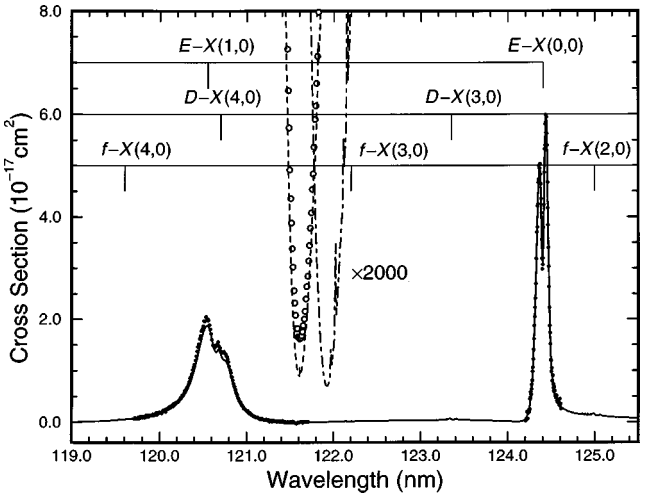

FIG. 5. Calculated and measured O_2 room-temperature cross sections. Experimental photoabsorption cross sections for the longest and second bands, $E\,^3\Sigma_u^-\leftarrow X\,^3\Sigma_g^-(0,0)$ and (1,0), (Refs. 40 and 41, solid circles) are compared with our calculated 297 K CSE Σ cross section for $^{16}O_2$ (the solid line). The positions of features arising from forbidden transitions into the $f\,^1\Sigma_u^+$ and $D\,^3\Sigma_u^+$ states are also indicated. In addition, with the aid of an expanded cross-section scale, the 288 K photoabsorption cross section of Lewis *et al.* (Ref. 5, open circles) is compared with our calculated 288 K CSE Σ cross section for $^{16}O_2$ (the dashed line). The calculated Σ cross section is significantly smaller than the measured total cross section at the cross-section minimum near 121.6 nm, indicating that the $O(^1D)+O(^3P)$ quantum yield is significantly less than unity (see the text). The calculated 288 K CSE Σ cross section for the $^{16}O^{18}O$ isotopomer (the dot-dashed line) is substantially greater than the $^{16}O_2$ cross section at Lyman-α and must be considered when estimating the quantum yield for normal O_2.

while the *f*-level block included the nine diabatic states of $^3\Sigma_{u1}^-$, $^3\Sigma_{u1}^+$, and $^3\Sigma_{u0}^+$ symmetry.

In this work, we concentrate mainly on a description of the $^3\Sigma_u^-$ model. In Fig. 4, the diabatic $^3\Sigma_u^-$ potential-energy curves $V_k(R)$ and $^3\Sigma_u^-\leftarrow X\,^3\Sigma_g^-$ electronic transition moments $\mathcal{M}_k(R)$ used in our CSE model are shown (dashed lines), together with the corresponding adiabatic potentials and transition moments (solid lines).[34] The diabatic electronic transition moments are taken to have a linear *R* dependence, while the Rydberg-valence couplings, 4033 and 2023 cm^{-1}, for $n=3$ and $n=4$, respectively, scaling approximately with $(n^*)^{-3/2}$,[24] are taken to be *R* independent.[35] While the diabatic $\hat{B}$-state valence potential-energy curve crosses the diabatic Rydberg curves, the strong electrostatic Rydberg-valence interaction in this basis results in adiabatic potential-energy curves which avoid crossing and are of heavily mixed character. In particular, the bound adiabatic *E*-state potential is a mixture of the pure valence and $n=3$ and $n=4$ Rydberg states. Conventionally, the lowest two vibrational levels of this *adiabatic* state are associated with the longest and second bands, the upper-state energies of which are shown in Fig. 4. However, it should be emphasized that neither the diabatic nor the adiabatic potential-energy curves exactly represent the observed energy levels and it is necessary to employ the CSE method to obtain realistic energies and cross sections. The adiabaticity parameter[36,37] for the lowest $^3\Sigma_u^-$ crossing is $\zeta\approx 1.3$, implying character intermediate between adiabatic and diabatic for the *E*-state levels in this region.

Initially, we calculated the room-temperature Σ cross section for $^{16}O_2$ defined by the CSE model described above, i.e., consisting essentially of the $^3\Sigma_u^-\leftarrow X\,^3\Sigma_g^-$ cross section, with minor features due to the $^3\Sigma_u^+$ and $^1\Sigma_u^+$ states, in the range 119.0–126.0 nm. First, using the diabatic upper-state potential-energy curves and couplings described above, the diabatic coupled-channel radial wave functions $\boldsymbol{\chi}_{\gamma EJ}(R)$, normalized according to the method of Mies,[25] were calculated by solving Eq. (9) using the renormalized Numerov method of Johnson.[38] Second, ground-state vibrational wave functions $\chi_{X0J''\Omega''}$, calculated using a Rydberg–Klein–Rees potential-energy curve for the $X\,^3\Sigma_g^-$ state constructed from the spectroscopic constants of Cosby,[39] together with the diabatic electronic transition moments of Fig. 4 and appropriate rotational matrix elements, were used with Eqs. (7) and (8) to calculate the individual rotational cross sections into the *e*- and *f*-level coupled-channel blocks, $\sigma_{EJ\leftarrow X0J''\Omega''}$. Third, forming appropriate ground-state wave functions for a Hund's coupling case intermediate between (a) and (b), and adding the *e*- and *f*-level cross sections while performing a Boltzmann average over the ground-state fine-structure levels, the final room-temperature Σ cross section was formed.

B. Results and discussion

In Fig. 5, the $^{16}O_2$ Σ cross section calculated for a temperature of 297 K is shown (the solid line), compared with experimental O_2 room-temperature photoabsorption cross sections measured for the longest[40] and second[41] bands (solid circles), $E\leftarrow X(0,0)$ and (1,0), respectively. Agreement between the calculations and measurements is excellent for

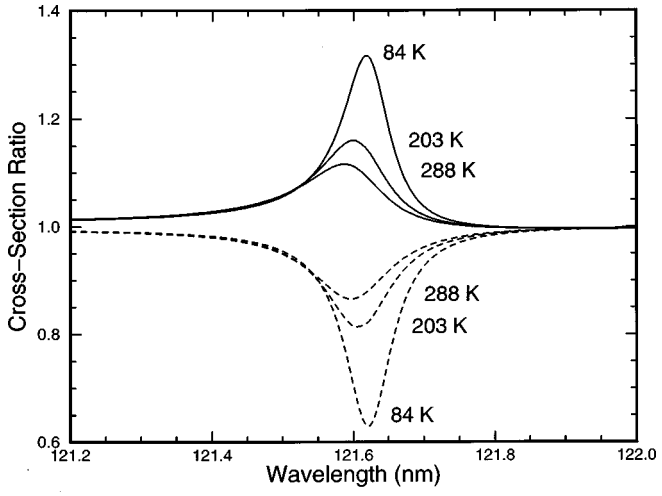

FIG. 6. The significance of second-order effects on the calculated cross sections for temperatures of 288, 203, and 84 K. Solid lines: Isotopic effect; ratios of the calculated Σ cross sections for normal O_2 and $^{16}O_2$. Dashed lines: Effect of indirect predissociation of the $^3\Sigma_u^-$ states by the $A\,^3\Sigma_u^+$ state; ratios of the calculated $\Sigma_{^1D}$ and Σ cross sections for $^{16}O_2$. Both effects are included in the calculated $O(^1D)$ quantum yields of Fig. 7.

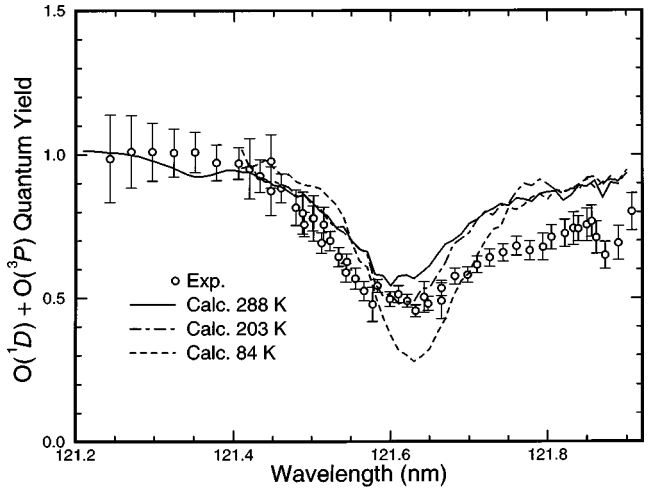

FIG. 7. Comparison between calculated and room-temperature experimental $O(^1D)+O(^3P)$ quantum-yield spectra for the photodissociation of O_2 near Lyman-α. Calculated quantum yields were obtained from our calculated CSE $\Sigma_{^1D}$ spectra, corrected for isotopic effects and shifted to longer wavelengths by 0.005 nm, and the experimental photoabsorption spectra of Refs. 5 and 22 (see the text for a discussion). The calculated minimum quantum yield, near 121.62 nm, decreases substantially as the temperature is lowered.

these very strong bands, with the largest discrepancy an ~5% underestimation of the cross section for the second band at ~120.6 nm. The positions of bands of the forbidden $f \leftarrow X$ and $D \leftarrow X$ systems are also indicated on Fig. 5. The most significant of these is the $D \leftarrow X(4,0)$ band which coincides with the second band, producing an interesting quantum-interference effect which will be discussed in detail elsewhere.[42] It is important to note that the excellent agreement between the calculated and measured structure on the long-wavelength wing of the second band would not have been possible without the inclusion of $^3\Sigma_u^+$ states in the CSE model.

Also shown in Fig. 5, with an expanded vertical scale, is the $^{16}O_2$ Σ cross section calculated for a temperature of 288 K in the region of Lyman-α (the dashed line), compared with the O_2 photoabsorption cross section, extrapolated to zero pressure, measured at the same temperature by Lewis *et al.*[5] (open circles). In this region, the measured cross section passes through a deep minimum, with a cross section some 10 000× smaller than at the peak of the longest band. The calculated Σ cross section also passes through a deep minimum at a similar wavelength, but this calculated minimum is significantly deeper than the measured minimum. This merely reflects the fact that we have calculated the Σ cross section, rather than the $\Sigma+\Pi$ cross section, and indicates that the $O(^1D)+O(^3P)$ quantum yield is significantly less than unity at the cross-section minimum. Rotational structure in the calculated Σ cross section at wavelengths longward of the minimum arises from the forbidden $f \leftarrow X(3,0)$ band.

The calculated $^{16}O^{18}O$ Σ cross section for $T=288$ K is also shown in Fig. 5 (the dot-dashed line). Due to a significant isotopic shift, the cross section for this isotopomer greatly exceeds that for $^{16}O_2$ at Lyman-α. The ratio of the calculated Σ cross sections for normal O_2 and $^{16}O_2$ is plotted in Fig. 6 (solid lines) as a function of wavelength near Lyman-α for temperatures of 84, 203, and 288 K.[43] The calculations show that, despite the low 0.408% abundance of $^{16}O^{18}O$, its effect on the photoabsorption of O_2 cannot be neglected, especially at low temperatures.

The effect of indirect predissociation of the $^3\Sigma_u^-$ states by the $A\,^3\Sigma_u^+$ state, foreshadowed in Sec. III A 2, can also be seen in Fig. 6 where the partial:total cross-section ratio $\sigma_{\Sigma_{^1D}}(\lambda)/\sigma_\Sigma(\lambda)$ for $^{16}O_2$ is plotted (dashed lines). This ''$O(^1D)$ Σ quantum yield'' decreases to values significantly below unity near Lyman-α, confirming the necessity of including $^3\Sigma_u^+$ states in the CSE model for an accurate description of the O_2 photodissociation in this region, especially at low temperatures.

In Fig. 7, our calculated $T=288$ K isotopically corrected $O(^1D)+O(^3P)$ quantum yield for the dissociation of O_2 (solid line) is shown as a function of wavelength in the Lyman-α region, 121.2–121.9 nm, in comparison with the measured room-temperature yield (open circles). The calculated yield was obtained from our isotopically corrected CSE $\Sigma_{^1D}$ cross section and a photoabsorption cross section constructed from the cross sections of Lewis *et al.*[5] and Dose *et al.*,[22] extrapolated to zero pressure. The calculated cross section was shifted to longer wavelengths by 0.005 nm before applying Eq. (11), in order to improve agreement with the measured position for the quantum-yield minimum. Such a small shift is within the wavelength uncertainty expected for the CSE calculations, and is not unreasonable considering the difficulties inherent in comparing calculated and experimental cross sections, each with its own uncertainty, in regions of rapidly varying cross section. The calculated quantum yield varies from 1.0 near 121.2 nm, passes through a minimum of 0.56 near 121.61 nm, and rises to 0.91 near 121.9 nm, in good agreement with the behavior of the measured quantum yield.

We have also studied the temperature dependence of the $O(^1D)+O(^3P)$ quantum yield in the range 121.4–121.9 nm by performing CSE calculations of the isotopically corrected

Σ_{1D} cross section for temperatures of 203 and 84 K, shifting to longer wavelengths by 0.005 nm, as above, and comparing with the 203 and 84 K measured photoabsorption cross sections of Lewis *et al.*[5] As can be seen in Fig. 7, the calculated quantum yields (the dot-dashed line and dashed line, respectively) exhibit deeper minima than at room temperature, with a minimum yield of 0.28 at 121.63 nm for $T=84$ K. This effect occurs because the Σ (and Σ_{1D}) cross sections in the deep minimum near H Lyman-α are very sensitive to the behavior of the wings of the nearby strong spectral features, and, as is quite usual, these wings are very temperature dependent. On the other hand, the Π cross section is only broadly structured in this region and is much less temperature dependent. Thus, the strong temperature effect for the quantum yield arises principally from the Σ cross section.

IV. CONCLUSIONS

The measured room-temperature $O(^1D)+O(^3P)$ quantum yield near Lyman-α deviates significantly from unity, going from 1.0 at 121.35 nm through a minimum of 0.48 near 121.62 nm. This behavior is reproduced by a coupled-channel Schrödinger-equations calculation, based principally on the $^3\Sigma_u^- \leftarrow X\,^3\Sigma_g^-$ transitions. The low $O(^1D)+O(^3P)$ quantum yield near Lyman-α implies a significant contribution to the O_2 photodissociation from $^3\Pi_u \leftarrow X\,^3\Sigma_g^-$ transitions which yield $O(^3P)+O(^3P)$.

A strong temperature dependence of the calculated quantum yield has been found, with a minimum yield of 0.28 near 121.63 nm at a temperature of 84 K. This strong dependence arises principally due to the temperature dependence of the $^3\Sigma_u^- \leftarrow X\,^3\Sigma_g^-$ cross section. In addition, it has been found that the cross section for $^{16}O^{18}O$ substantially exceeds the $^{16}O_2$ cross section near Lyman-α, implying that the heteronuclear isotopomer plays a nonnegligible role in the photodissociation of normal O_2 in this wavelength region.

The results of the present work will help in modeling more accurately the effects of $O(^1D)$ generated from O_2 photodissociation by solar Lyman-α radiation in the mesosphere and lower thermosphere. It would be interesting to verify experimentally the temperature dependence of the $O(^1D)$ yield, given the broad temperature range (170–250 K) prevailing in the mesosphere and lower thermosphere.

ACKNOWLEDGMENTS

The experimental portion of this work was supported by NASA's Sun-Earth Connection Program. The authors thank Professor J. H. Carver for a critical reading of the manuscript.

[1] Throughout this work, Lyman-α is taken to mean H Lyman-α.
[2] G. Brasseur and S. Solomon, *Aeronomy of the Middle Atmosphere* (Reidel, Dordrecht, 1984), pp. 154–160.
[3] L. C. Lee, T. G. Slanger, G. Black, and R. L. Sharpless, J. Chem. Phys. **67**, 5602 (1977).
[4] S. Chabrillat and G. Kockarts, Geophys. Res. Lett. **24**, 2659 (1997).
[5] B. R. Lewis, I. M. Vardavas, and J. H. Carver, J. Geophys. Res. **88**, 4935 (1983).
[6] T. N. Woods and G. J. Rottman, J. Geophys. Res. **102**, 8769 (1997).
[7] W. K. Tobiska, W. R. Pryor, and J. M. Ajello, Geophys. Res. Lett. **24**, 1123 (1997).
[8] R. R. Meier and D. K. Prinz, J. Geophys. Res. **75**, 6969 (1970).
[9] S. A. Meyer and G. W. Faris, Opt. Lett. **23**, 204 (1998).
[10] In this work, energies in electron-volts are referred to the minimum in the ground-state $X\,^3\Sigma_g^-$ potential-energy curve.
[11] B. A. Ridley, R. Atkinson, and K. H. Welge, J. Chem. Phys. **58**, 3878 (1973).
[12] N. K. Bibinov, I. P. Vinogradov, and A. M. Pravilov, Opt. Spectrosc. **53**, 496 (1982).
[13] G. M. Lawrence and M. J. McEwan, J. Geophys. Res. **78**, 8314 (1973).
[14] One may, of course, speak of the ''$O(^1D)$ yield'' as a short form for the $O(^3P)+O(^1D)$ yield. These two forms are used interchangeably throughout this work.
[15] Chemical Kinetics and Photochemical Data for Use in Stratospheric Modeling, Evaluation Number 12, JPL Publication No. 97-4, NASA, January 15, 1997.
[16] M. J. E. Gauthier and D. R. Snelling, Can. J. Chem. **52**, 4007 (1974).
[17] H. I. Bloemink, R. A. Copeland, and T. G. Slanger, J. Chem. Phys. **109**, 4237 (1998).
[18] L. C. Lee and T. G. Slanger, J. Chem. Phys. **69**, 4053 (1978).
[19] I. Dabrowski, Can. J. Phys. **62**, 1639 (1984).
[20] G. W. Faris and M. J. Dyer, Opt. Lett. **18**, 382 (1993).
[21] M. R. Taherian and T. G. Slanger, J. Chem. Phys. **83**, 6246 (1985).
[22] V. Dose, U. Schmocker, and G. Sele, Z. Phys. A **274**, 1 (1975).
[23] M. Nicolet, Planet. Space Sci. **33**, 69 (1985).
[24] H. Lefebvre-Brion and R. W. Field, *Perturbations in the Spectra of Diatomic Molecules* (Academic, Orlando, 1986), pp. 56, 209–212.
[25] F. H. Mies, Mol. Phys. **41**, 953 (1980).
[26] E. F. van Dishoeck, M. C. van Hemert, A. C. Allison, and A. Dalgarno, J. Chem. Phys. **81**, 5709 (1984).
[27] L. Torop, D. G. McCoy, A. J. Blake, J. Wang, and T. Scholz, J. Quant. Spectrosc. Radiat. Transf. **38**, 9 (1987).
[28] J. P. England, B. R. Lewis, S. T. Gibson, and M. L. Ginter, J. Chem. Phys. **104**, 2765 (1996).
[29] B. R. Lewis, S. S. Banerjee, and S. T. Gibson, J. Chem. Phys. **102**, 6631 (1995).
[30] J. Wang, D. G. McCoy, A. J. Blake, and L. Torop, J. Quant. Spectrosc. Radiat. Transf. **38**, 19 (1987).
[31] J. Wang, A. J. Blake, D. G. McCoy, and L. Torop, J. Quant. Spectrosc. Radiat. Transf. **40**, 501 (1988).
[32] Y. Tanaka, J. Chem. Phys. **20**, 1728 (1952).
[33] B. R. Lewis, S. T. Gibson, J. P. England, and M. L. Ginter (unpublished).
[34] We use the *caret* to distinguish the pure diabatic electronic state (e.g., $\hat{B}$) from the corresponding adiabatic electronic state (e.g., B), with the convention that the diabatic and adiabatic states become indistinguishable at large R where the coupling is taken to approach zero.
[35] The $n=3$ Rydberg-valence couplings for the $^1\Sigma_u^+$ and $^3\Sigma_u^+$ states were ~ 1600 and ~ 400 cm^{-1}, respectively [S. S. Banerjee, Ph.D. dissertation thesis, The Australian National University, 1997.] These smaller couplings, and the high-energy location of the $^1\Sigma_u^+$ valence state, cause the lower vibrational structures of the $3p\pi_u f\,^1\Sigma_u^+$ and $3p\pi_u D\,^3\Sigma_u^+$ Rydberg states to be relatively unperturbed by the Rydberg-valence interactions, especially when compared with the highly perturbed $E\,^3\Sigma_u^-$ vibrational structure.
[36] K. Dressler, Ann. Isr. Phys. Soc. **6**, 141 (1983).
[37] The adiabaticity parameter $\zeta = V_{\hat{B}\hat{E}}/\Delta G_E$, where $V_{\hat{B}\hat{E}}$ is the electrostatic interaction matrix element between the diabatic electronic states, and ΔG_E is the separation of the first levels of the upper adiabatic state formed by the avoided crossing. This parameter provides a measure of the applicability of the adiabatic or diabatic picture to the mixed states. Near adiabatic behavior occurs for $\zeta \gg 1$, near-diabatic behavior for $\zeta \ll 1$, while for $\zeta \approx 1$, the amount of basis-state mixing in either representation is large.
[38] B. R. Johnson, J. Chem. Phys. **69**, 4678 (1978).
[39] P. C. Cosby (private communication).
[40] B. R. Lewis, S. T. Gibson, M. Emami, and J. H. Carver, J. Quant. Spectrosc. Radiat. Transf. **40**, 1 (1988).
[41] B. R. Lewis (unpublished).
[42] S. T. Gibson, B. R. Lewis, and D. G. McCoy (unpublished).
[43] The cross section for normal O_2 was estimated as an average of the Σ cross sections for $^{16}O_2$ and $^{16}O^{18}O$, weighted in the ratio 0.995 92:0.004 08, respectively.